A Model for Pleiotropic Muscarinic Potentiation of Fast Synaptic Transmission

Hermann Schobesberger, Diek W. Wheeler and John P. Horn

JN 83:1912-1923, 2000.

Journal of Neurophysiology publishes original articles on the function of the nervous system. It is published 12 times a year (monthly) by the American Physiological Society, 9650 Rockville Pike, Bethesda MD 20814-3991. ISSN: 0022-3077, ESSN: 1522-1598. Visit our website at http://www.the-aps.org/.

A Model for Pleiotropic Muscarinic Potentiation of Fast Synaptic Transmission

HERMANN SCHOBESBERGER, DIEK W. WHEELER, AND JOHN P. HORN
Department of Neurobiology, University of Pittsburgh School of Medicine, Pittsburgh, Pennsylvania 15261

Schobesberger, Hermann, Diek W. Wheeler, and John P. Horn. A model for pleiotropic muscarinic potentiation of fast synaptic transmission. *J. Neurophysiol.* 83: 1912–1923, 2000. The predominant form of muscarinic excitation in the forebrain and in sympathetic ganglia arises from m1 receptors coupled to the $G_{q/11}$ signal transduction pathway. Functional components of this system have been most completely mapped in frog sympathetic B neurons. Presynaptic stimulation of the B neuron produces a dual-component muscarinic excitatory postsynaptic potential (EPSP) mediated by suppression of voltage-dependent M-type K^+ channels and activation of a voltage-insensitive cation current. Evidence from mammalian systems suggests that the cation current is mediated by cyclic GMP-gated channels. This paper describes the use of a computational model to analyze the consequences of pleiotropic muscarinic signaling for synaptic integration. The results show that the resting potential of B neurons is a logarithmic function of the leak conductance over a broad range of experimentally observable conditions. Small increases (<4 nS) in the muscarinically regulated cation conductance produce potent excitatory effects. Damage introduced by intracellular recording can mask the excitatory effect of the muscarinic leak current. Synaptic activation of the leak conductance combines synergistically with suppression of the M-conductance ($40 \rightarrow 20$ nS) to strengthen fast nicotinic transmission. Overall, this effect can more than double synaptic strength, as measured by the ability of a fast nicotinic EPSP to trigger an action potential. Pleiotropic muscarinic excitation can also double the temporal window of summation between subthreshold nicotinic EPSPs and thereby promote firing. Activation of a chloride leak or suppression of a K^+ leak can substitute for the cation conductance in producing excitatory muscarinic actions. The results are discussed in terms of their implications for synaptic integration in sympathetic ganglia and other circuits.

INTRODUCTION

Muscarinic synapses regulate activity throughout the nervous system, from the cerebral cortex to peripheral autonomic ganglia. When muscarinic transmission in the forebrain is impaired by drugs, or by neurodegenerative disorders such as Alzheimer's disease, the cognitive effects include memory loss and dementia (Lawrence and Sahakian 1998; Levey 1996; Perry et al. 1999; Winkler et al. 1998). Although these profound behavioral phenomena remain poorly understood in terms of the underlying neural circuitry, there is considerable evidence that cholinergic pathways play a modulatory role in the cortex. The case for modulation rests largely on the diffuse anatomic organization of central cholinergic pathways and the modulatory influence of muscarinic receptors on voltage-dependent ion channels (Brown et al. 1997; Caulfield 1993; Descarries et al. 1997; Hasselmo 1995). Advancing to the next level of analysis poses a more difficult challenge. Three experimental problems generally arise whenever one attempts to relate the molecular details of muscarinic modulation to neural circuit dynamics. First, muscarinic receptors often regulate multiple ionic conductances through complex transduction pathways, whose frequent branch points and intersections are difficult to dissect. It therefore remains generally unclear how the subcomponents of a muscarinic response combine to influence synaptic integration. Second, muscarinically controlled conductance changes can be quite small and comparable in magnitude to perturbations introduced by intracellular recording. This suggests that recording damage may confound experiments by obscuring the normal influence of muscarinic modulation. Third, it remains difficult to activate muscarinic synapses selectively, even in brain slices, and thereby test how they modulate other synapses (Cole and Nicoll 1983, 1984; Madison et al. 1987). Here, we solve these three generic problems by considering sympathetic ganglia, a system whose relative simplicity facilitates experimentation and the building of computational models.

In paravertebral sympathetic ganglia one can resolve several distinct muscarinic mechanisms and observe how they interact with fast ionotropic synapses. The cell-specific expression of muscarinic synapses has been defined most clearly in bullfrog sympathetic ganglia, where preganglionic activity drives two forms of synaptic inhibition (Dodd and Horn 1983b; Horn and Dodd 1981; Shen and Horn 1996) and a slow excitatory postsynaptic potential (EPSP) (Nishi and Koketsu 1968; Tosaka et al. 1968). This paper focuses on the excitatory mechanism.

The pleiotropic nature of muscarinic excitation has been studied extensively in sympathetic neurons of the frog and rat, and in sympathetically derived neuroblastoma cell lines. Muscarinic agonists depolarize B neurons in frog ganglia by suppressing voltage-dependent M-potassium channels (g_M) and by increasing a background leak conductance (g_{leak}) (Adams and Brown 1982; Akasu et al. 1984; Brown and Adams 1980; Jones 1985; Kuba and Koketsu 1974; Kuffler and Sejnowski 1983; Tsuji and Kuba 1988). In rat sympathetic neurons and in the NG108–15 cell line, it has been further determined that m1-type receptors regulate M-current through the $G_{q/11}$ protein (Caulfield 1993). Although this pathway also activates phospholipase C and releases Ca^{2+} from intracellular stores, the role of these effects in channel regulation remains controversial (Marrion 1997). Nonetheless, there has been considerable recent progress in identifying the protein subunits that form the

The costs of publication of this article were defrayed in part by the payment of page charges. The article must therefore be hereby marked "*advertisement*" in accordance with 18 U.S.C. Section 1734 solely to indicate this fact.

M-channel (Selyanko et al. 1999; Wang et al. 1998) and in identifying modulatory effects of Ca^{2+}on M-channel gating (Marrion 1996, 1997; Selyanko and Brown 1996). Comparatively less is known about the increase in g_{leak} during muscarinic excitation. In frog B neurons, the muscarinic g_{leak} appears to be cation selective, voltage-insensitive, and relatively small (<7 nS), and it is thought to exert little influence on excitability (Jones 1985; Kuba and Koketsu 1974; Tsuji and Kuba 1988). Other work suggests that the muscarinic g_{leak} may be mediated by cyclic nucleotide-gated cation channels (g_{CNG}). In N1E-115 neuroblastoma, muscarinic excitation stimulates intracellular Ca^{2+} release, Ca^{2+}-sensitive synthesis of nitric oxide, accumulation of cyclic GMP, and activation of g_{CNG} (Mathes and Thompson 1996; Thompson 1997; Trivedi and Kramer 1998). This might explain earlier studies of mammalian sympathetic neurons, which localized nitric oxide synthase in cell bodies (Sheng et al. 1993) and showed an indirect association between the muscarinic elevation of cyclic GMP, depolarization, and increased background conductance (Ariano et al. 1982; Briggs et al. 1982; Hashiguchi et al. 1978; Kebabian et al. 1975a,b; McAfee and Greengard 1972). Contemporaneous experiments on frog sympathetic ganglia also demonstrated muscarinic stimulation of cyclic GMP accumulation but failed to detect any electrophysiological consequences (Weight et al. 1974, 1978). In hindsight, it is clear that all of these pioneering studies were hampered by the technical difficulty of measuring small conductance changes.

Our goal in developing a conductance-based model was to circumvent the problems introduced by recording damage and explore the consequences of dual-component muscarinic excitation. How do g_M and g_{CNG} interact with fast nicotinic transmission to initiate action potentials? The answer to this question has broad implications for understanding sympathetic circuit function. It has recently been discovered that >90% of frog B neurons are multiply innervated by axons forming one strong connection and one to four weak connections, respectively dubbed as primary and secondary nicotinic synapses (Karila and Horn 2000). Although secondary EPSPs are generally subthreshold in strength, they can trigger action potentials through summation or by interaction with a slow peptidergic EPSP. The conductance changes that mediate peptidergic excitation of frog B neurons appear identical to those controlled by muscarinic receptors (Jones 1985; Katayama and Nishi 1982; Kuffler and Sejnowski 1983). These observations have all been incorporated into a stochastic theory, whose central prediction is that sympathetic ganglia function as variable synaptic amplifiers of preganglionic activity (Karila and Horn 2000). The theory further predicts that slow muscarinic and peptidergic EPSPs increase synaptic gain by enhancing the strength of secondary nicotinic synapses and by lengthening the temporal window of summation between secondary EPSPs. The model that we now describe explains how changes in g_M and g_{CNG} combine synergistically to promote synaptic amplification in sympathetic ganglia.

METHODS

The simple monopolar shape of frog sympathetic B neurons makes them electrotonically compact (Yamada et al. 1989). The model cell we studied had a single isopotential compartment and followed the Hodgkin-Huxley formalism. In the master equation (*Eq. 1*), the sum of all ionic currents (I_{ionic}), together with the capacitive current (C = membrane capacitance; V = membrane potential; t = time), is equal to the current injected through an intracellular electrode ($I_{injected}$). Under normal physiological conditions, in the absence of an electrode, $I_{injected} = 0$. We assumed a specific membrane capacitance of 1 $\mu F/cm^2$ and set C to 100 pF, which corresponds to a spherical cell with a radius of 28.2 μm. This falls within the observed size range of living B cells taken from adult bullfrogs (4–6 in. body length) (Dodd and Horn 1983a) and agrees with experimental measurements of their membrane capacitance (Jones 1987)

$$I_{ionic} + C\frac{dV}{dt} = I_{injected} \quad (1)$$

Our computational model was patterned after a molecular hypothesis. Figure 1*A* outlines the mechanism that may account for the transduction of dual component muscarinic excitation in frog sympathetic B neurons, and Fig. 1*B* illustrates the equivalent electrical circuit for our computational model. Eight parallel pathways were used to describe the capacitive and ionic currents. The ionic currents were carried by three types of voltage-insensitive leak conductance, an M-type K^+ conductance (g_M), a fast nicotinic synaptic conductance (g_{syn}), a fast inactivating Na^+ conductance (g_{Na}), and a delayed-rectifier K^+ conductance (g_K). Each ionic current obeyed Ohm's law. In generic notation (*Eq. 2*), i_a is the current through conductance a, $\bar{g}_a$ is the maximal conductance, E_a is the reversal potential, and A is a gating variable. The value of A can range between 0 and 1 as a function of voltage, time, or transmitter action

$$i_a = \bar{g}_a A(V - E_a) \quad (2)$$

Leak conductances

The three components of leak conductance included a background leak (g_{leak}) that helps set the resting membrane potential, a damage leak (g_{elec}) introduced by an intracellular recording electrode, and a cyclic nucleotide–gated leak (g_{CNG}) controlled by muscarinic receptors. The magnitude of each conductance and the associated reversal potentials were varied as required for different simulations. Because all the leak conductances are voltage insensitive and remain constant over the time scale of fast EPSPs and action potentials (i.e., $A = 1$), they sum linearly (*Eq. 3*), and their net reversal potential ($E_{leak-total}$) is given by a chord conductance equation (*Eq. 4*)

$$g_{leak-total} = g_{leak} + g_{elec} + g_{CNG} \quad (3)$$

$$E_{leak-total} = \frac{g_{leak}E_{leak} + g_{elec}E_{elec} + g_{CNG}E_{CNG}}{g_{leak-total}} \quad (4)$$

M-conductance

The M-current was modeled using the same kinetic scheme (*Eqs. 5–8*) that was originally developed to describe voltage-clamp currents recorded from B neurons (Adams et al. 1982; Yamada et al. 1989). We generally set $\bar{g}_M = 40$ nS and $E_K = -90$ mV, based on whole cell recordings from dissociated B neurons (Jones 1989). Exceptions are found in Fig. 4, *B* and *D*

$$i_M = \bar{g}_M \omega (V - E_K) \quad (5)$$

$$\frac{d\omega}{dt} = \frac{\omega_\infty - \omega}{\tau_\omega} \quad (6)$$

$$\tau_\omega = \frac{1{,}000}{3.3[e^{(V+35)/40} + e^{-(V+35)/20}]} \quad (7)$$

$$\omega_\infty = \frac{1}{1 + e^{-(V+35)/10}} \quad (8)$$

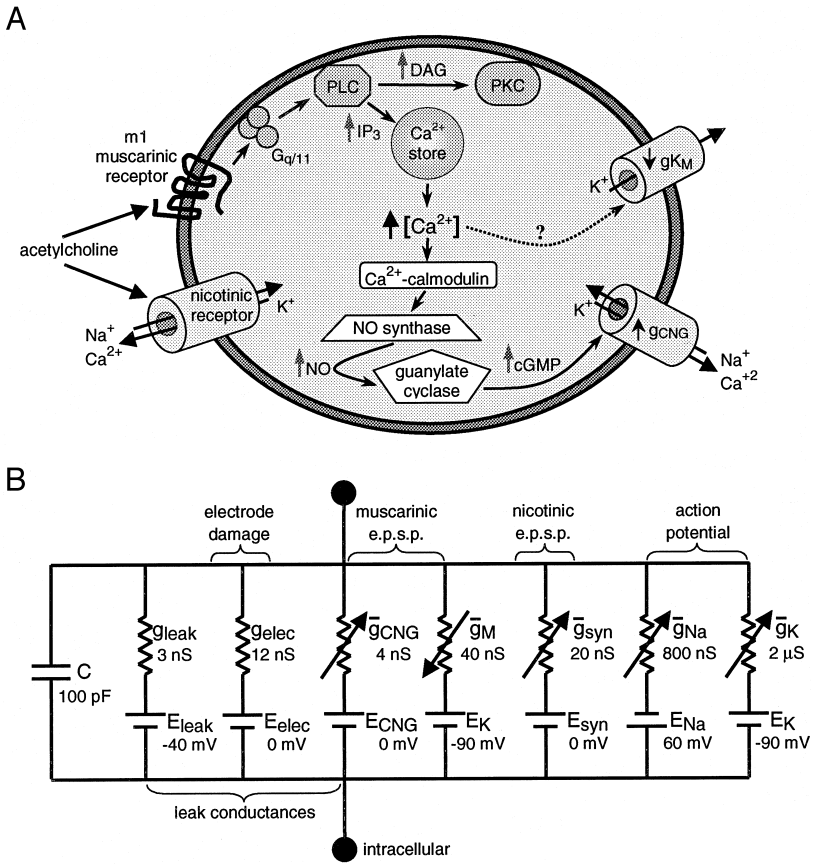

FIG. 1. Molecular (*A*) and electrical (*B*) models of muscarinic excitation. *A*: acetylcholine excites sympathetic neurons by coactivating nicotinic and muscarinic receptors that produce fast and slow excitatory postsynaptic potentials (EPSPs). The diagram summarizes a working hypothesis for pleiotropic muscarinic suppression of g_M and activation of a cation conductance. The intracellular pathway is a composite based on evidence from different preparations of sympathetic neurons and neuroblastoma cell lines. Cyclic GMP–gated channels (g_{CNG}) are hypothesized to mediate the muscarinic cation conductance in frog B neurons. The possibility that intracellular Ca^{2+} regulates g_M is supported by some experiments, but the issue remains controversial. DAG, diacyl glycerol; IP_3, inositol tris phosphate; NO, nitric oxide; PKC, protein kinase C; PLC, phospholipase C. *B*: the equivalent electrical circuit used to model the frog sympathetic B neuron. A minimum of 7 conductances are required to account for the influence of damage produced by intracellular recording and to examine the muscarinic modulation fast synaptic transmission in terms of postsynaptic excitability.

Fast nicotinic conductance

The fast nicotinic EPSP was modeled by calculating a synaptic current (*Eq. 9*) and scaling it with a kinetic template (*Eq. 10*). The template (s_t) was created (Fig. 2*A*) by inverting a synaptic current recorded at −60 mV (taken from Fig. 6*A* in Shen and Horn 1995), scaling the peak to a dimensionless value of 1, and fitting the resultant waveform with the sum of two exponentials (t = time in ms). E_{syn} was set to 0 mV (Shen and Horn 1995), and $\bar{g}_{syn}$ was varied as a free parameter

$$i_{syn} = \bar{g}_{syn} s_t (V - E_{syn}) \quad (9)$$

$$s_t = 1.869(e^{-t/5} - e^{-t}) \quad (10)$$

Action potential

To assess the strength of nicotinic synapses, we modeled a simplified action potential mechanism whose threshold (−37 mV) was physiologically realistic (Jones 1987; Karila and Horn 2000). The action potential was constructed from two conductances that control a fast Na^+ current (*Eq. 11*, *m* activation, *h* inactivation) and a delayed-rectifier K^+ current (*Eq. 12*, *n* activation, *p* inactivation)

$$i_{Na} = \bar{g}_{Na} m^2 h (V - E_{Na}) \quad (11)$$

$$i_K = \bar{g}_K n^2 p (V - E_K) \quad (12)$$

Sodium currents in B neurons have two kinetically and pharmacologically distinct components whose complexity has hampered efforts to describe them in quantitative terms (Jones 1987). We therefore used the rate equations that Yamada et al. (1989) employed to model the voltage dependence and time dependence of *m* and *h*. Their idea of raising *m* to the second power (*Eq. 11*) and the form of the four rate constants that control *m* and *h* were all derived from an earlier model describing Na^+ currents in the amphibian node of Ranvier (Frankenhaeuser and Huxley 1964). Because the action potential is slower in B neurons than in the node, Yamada et al. (1989) slowed down i_{Na} in the model. We followed their kinetic modifications in which the time constants of activation and inactivation were doubled, and other changes were made to produce a positive shift in the voltage dependence of activation. We set $\bar{g}_{Na}$ = 800 nS and E_{Na} = +60 mV, to lie within the range of experimental measurements (Jones 1987). Figure 2*B* illustrates a family of simulated Na^+ currents evoked by depolarizing steps from a holding potential of −60 mV. As is typical of Na^+ currents in general, the rates of activation and inactivation both increase with depolarization. More specifically, however, the magnitude, time course (Fig. 2*B*), voltage dependence (Fig. 2*E*), and activation (Fig. 2*F*) of the simulated Na^+ currents reproduced the basic behavior of whole cell Na^+ currents recorded from B neurons (Jones 1987).

The delayed rectifier ($\bar{g}_K$ = 2 µS) in our model was based on the original experimental analysis in B neurons (Adams et al. 1982) and had kinetics similar to those described by Yamada et al. (1989). In B neurons, the activation of g_K is best fit by *n* squared (Adams et al. 1982; Block and Jones 1996; Klemic et al. 1998). We followed the convention of shifting the voltage dependence of n_∞ by 20 mV (Yamada et al. 1989) to better align it with the experimental data (see Fig. 16 in Adams et al. 1982). Although g_K does not inactivate in B neurons (Adams et al. 1982; Block and Jones 1996; Klemic et al. 1998), we examined the effect of including an inactivation process (Fig. 2, *C* and *D*) that was patterned after the node of Ranvier (Yamada et al. 1989). Inactivation (*p*) systematically lowered the maximum i_K at all voltages (Fig. 2, *E* and *F*), but its inclusion in the model had negligible effect on the action potential threshold (0.1 mV) and did not alter the results.

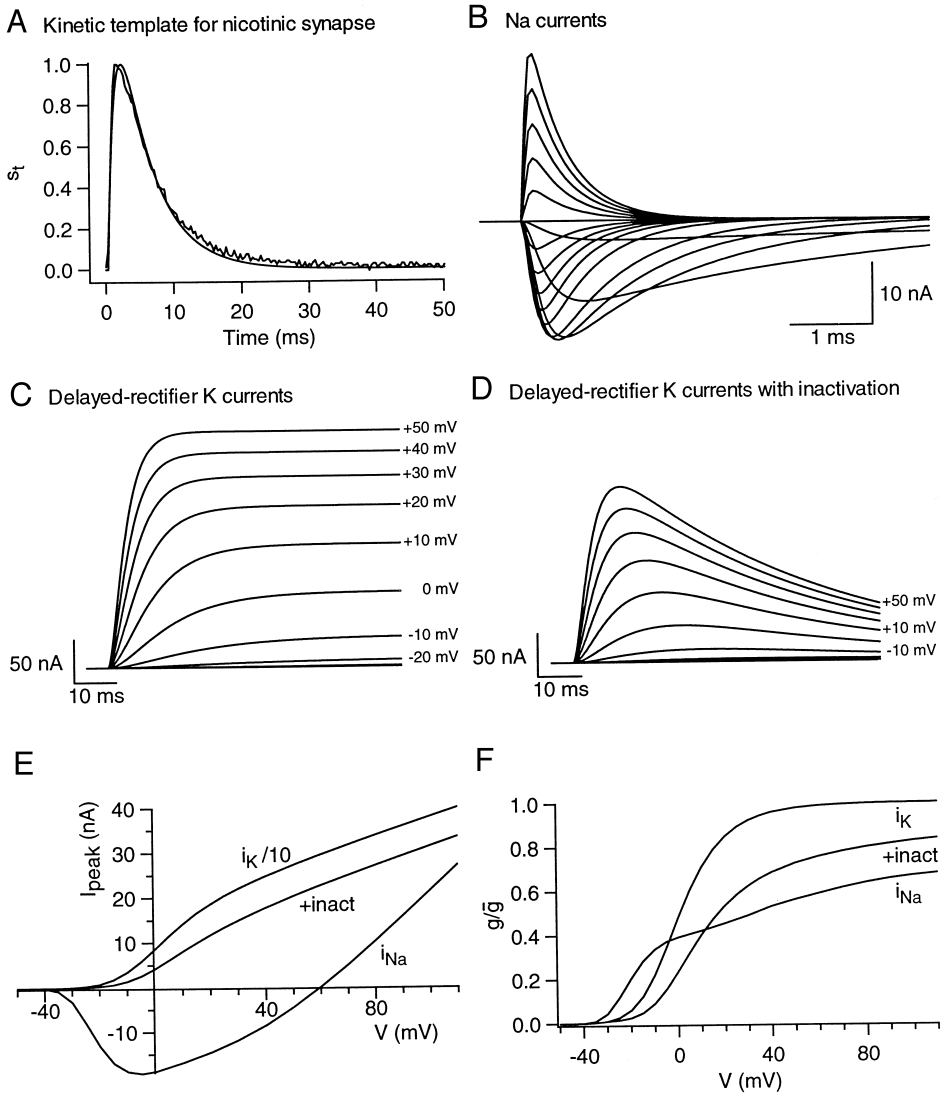

FIG. 2. Currents underlying the simulated nicotinic EPSP and action potential. *A*: the fast nicotinic EPSP was computed using a kinetic template (s_t) that described the time course of the synaptic current (*Eq. 10*). The template was created by fitting a curve to an inverted synaptic current (noisy trace). The excitatory postsynaptic current (EPSC) was recorded from a B neuron at a holding potential of −60 mV. *B*: fast Na^+ currents computed from *Eq. 11*. Membrane potential was held at −60 mV and depolarized in steps to values ranging from −30 to +110 mV. *C*: delayed-rectifier K^+ currents computed from *Eq. 12* without inactivation ($P = 1$). Holding potential = −60 mV. Membrane potential during step depolarization is indicated at the right of each trace. *D*: effect of inactivation on delayed rectifier currents. This family of currents was computed using the same clamp voltages shown in *C*. Introducing inactivation clips the peak K^+ current at each voltage. *E*: current-voltage relations for peak currents carried by g_{Na}, g_K, and g_{Kp} (with inactivation). For the purpose of display, the K^+ currents were divided by 10. *F*: activation curves for g_{Na} and g_K. At each voltage the computed ionic conductance was normalized to the maximal conductance ($\bar{g}$).

Numerical integration

The system of ordinary differential equations (ODE) that describes the model was numerically integrated on a 300-MHz Pentium II computer (WinNT4.0) using an implicit fourth-order Runge-Kutta algorithm. The procedure was implemented with phase-plane software (WinPP, written by Dr. G. Bard Ermentrout, ftp://ftp.math.pitt.edu/pub/bardware). The model is available in executable ODE files (http://horndell9goldi.neurobio.pitt.edu). WinPP permits integration with a fixed or variable time step. We compared both methods and found that the variable time step was not appreciably faster, presumably due to the model's simplicity. The standard approach for integrating equations was therefore to choose a constant time step that gave correct solutions and convenient resolution. In simulations to construct current-voltage (*I-V*) relations (i.e., Figs. 3 and 4), a time step of 0.25 ms was adequate. Brief intervals (50 μs) were used in simulations that contained synaptic potentials and action potentials (i.e., Figs. 5–7).

Voltage-clamp currents were simulated by setting d*V*/d*t* to 0 (*Eq. 1*), making *V* the independent variable, and solving for I_{ionic}. *I-V* relations were generated by controlling *V* with a step function of variable amplitude. In current-clamp simulations, a software flag was used to trigger the kinetic template (s_t) for the nicotinic synapse, and *Eq. 1* was solved for *V*. Illustrations were prepared using Igor 3.14 (PC edition, Wavemetrics, Lake Oswego, OR).

RESULTS

Importance of the leak conductance

The first task in constructing the model B neuron was to select parameters that reproduce experimentally observed resting behavior. In the voltage range between −40 and −80 mV, the steady-state *I-V* relation of the frog B neuron is dominated by M-current and a leak current (Adams et al. 1982; Jones 1989). Consequently, g_M and g_{leak} are both critical for controlling the resting potential (V_{rest}) and input resistance (R_{in}). In practice, these resting properties are difficult to measure accurately because intracellular recording perturbs the leak. We therefore began by examining the interplay between g_M, g_{leak}, and recording damage.

Variation in the data describing B neurons serves to define the parameter space for the model. It was estimated originally that $\bar{g}_M = 84$ nS, $g_{leak} = 10$ nS, and $E_{leak} = -10$ mV (Adams et al. 1982). This work employed two-electrode recordings to voltage-clamp large B neurons ($C = 150–400$ pF) in isolated ganglia. Subsequent whole cell patch recordings from smaller dissociated B neurons ($C = 75$ pF) yielded lower values for all three parameters ($\bar{g}_M = 27–37$ nS, $g_{leak} = 3–5$ nS, $E_{leak} = -55$

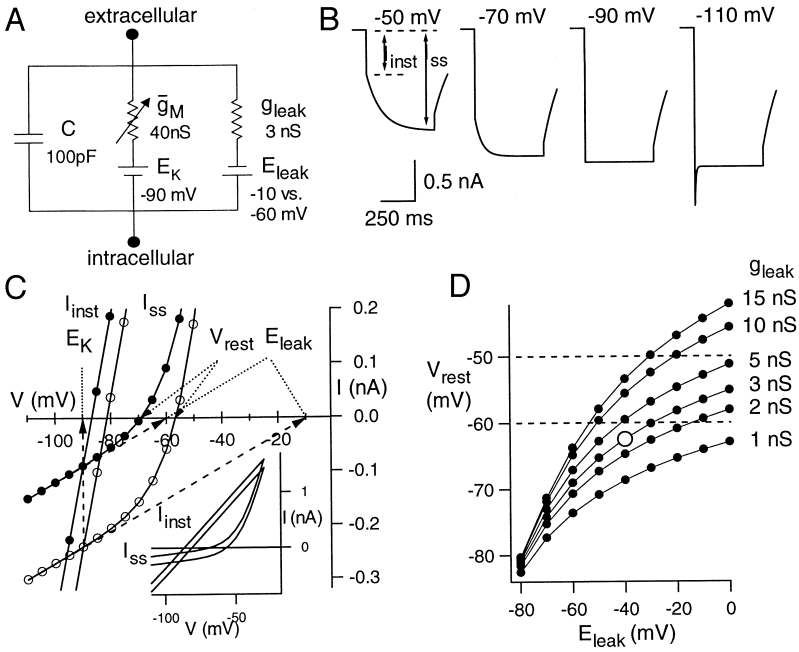

FIG. 3. Two-conductance model of the bullfrog sympathetic B neuron. *A*: circuit diagram of the model. *B*: simulated voltage-clamp currents evoked by voltage steps from holding potential of −30 mV. In each response the instantaneous current (I_{inst}) reflects membrane conductance at −30 mV, and the slowly relaxing inward current reflects voltage-dependent closure of M channels (I_M). Steady-state current (I_{ss}) is the sum of $I_{inst} + I_M$. On repolarization, I_{inst} is smaller because total membrane conductance is reduced. As in physiological recordings (Adams et al. 1982a; Jones 1989), I_M speeds up with hyperpolarization and reverses at E_K. *C*: instantaneous and steady-state *I-V* relations constructed from families of voltage-clamp currents (●, E_{leak} = −60 mV; ○, E_{leak} = −10 mV). The depolarizing shift in E_{leak} produces a 150-pA inward shift in all currents. This depolarizes V_{rest} and increases input conductance (slope of I_{ss} at V_{rest}). *Inset*: full *I-V* relations. *D*: plots of V_{rest} vs. E_{leak} at different values of g_{leak}. The open symbol (○) denotes background leak values (3 nS, −40 mV) used in subsequent simulations of interactions between nicotinic and muscarinic synapses. These conservative starting assumptions set V_{rest} slightly higher than generally recorded with microelectrodes (Adams and Harper 1995) (– – –). None of the subsequent conclusions depends critically on these specific resting conditions.

to −75 mV) (Jones 1989). Using these different data sets, Adams et al. (1982) calculated that V_{rest} = −53 mV, and R_{in} = 42 MΩ, whereas Jones (1989) estimated that $V_{rest} \approx$ −65 to −75 mV, and $R_{in} \approx$ 300 MΩ. The discrepancies presumably arise from differences in cell size, the larger shunt conductance (g_{elec}) introduced by dual microelectrodes, and the perturbations caused by tissue culture and whole cell dialysis. However, after normalizing the conductance data for cell size by dividing it by *C*, the most striking difference is in the leak selectivity (E_{leak}).

To analyze the influence of E_{leak}, voltage-clamp currents and *I-V* relations were simulated in a two-conductance model B neuron (Fig. 3*A*) of intermediate size (diameter = 56 μm, *C* = 100 pF). We set $\bar{g}_M$ = 40 nS, which gives a conductance density of 0.4 nS/pF and falls within the range of the whole cell data (0.36–0.49 nS/pF). The leak parameters were initially set as g_{leak} = 3 nS and E_{leak} = −60 mV, consistent with minimal damage in the best patch recordings. Using these parameters, we simulated a family of voltage-clamp currents (Fig. 3*B*) by following a typical experimental protocol for constructing *I-V* relations and measuring g_M. The membrane was held at −30 mV, where 62% of g_M is activated (*Eq. 8*), and was stepped systematically to hyperpolarized potentials. Each response begins with an instantaneous current (I_{inst}) whose magnitude reflects the membrane conductance at the holding potential and the amplitude of the voltage step. I_{inst} is followed by a slowly relaxing current caused by deactivation of g_M. I_M relaxes more rapidly at hyperpolarized potentials and reverses polarity at −90 mV, which is E_K (Fig. 3*B*). The steady-state current (I_{ss}) at the end of the test pulse reflects the new conductance. On repolarization the instantaneous current is reduced, thereby showing that total membrane conductance decreases during the hyperpolarizing test pulse. Plotting I_{inst} and I_{ss} as functions of *V* completes the task of reproducing the classical experimental findings (compare Fig. 3*C* with Fig. 5 in Adams et al. 1982; and Fig. 1 in Jones 1989). Graphic analysis of the simulated *I-V* data provided a check for internal consistency of the model by testing its ability to recover starting parameters (Fig. 3*C*). At potentials negative to −80 mV, where g_M is completely deactivated, the linear slope (3 nS) of the steady-state *I-V* relation reflects g_{leak}, and extrapolation correctly reveals its ionic selectivity ($x_{intercept} = E_{leak}$). The K^+ selectivity of g_M is recovered from the intersection between I_{inst} and I_{ss} at −90 mV. Activation of g_M (*Eq. 8*) introduces curvature into the steady-state *I-V* relation at potentials positive to −80 mV.

We could now dissociate the influence of leak selectivity from that of leak magnitude. Holding g_{leak} constant, E_{leak} was changed from −60 to −10 mV to reproduce the disparity between the microelectrode and patch recording data. The 50-mV shift in E_{leak} had no effect on the form of clamp currents evoked by voltage jumps (Fig. 3*B*) but offset their baselines by 150 pA. The offset was evident as a parallel inward shift in the steady-state and instantaneous *I-V* relations (Fig. 3*C*). The inward current depolarized V_{rest} from −69 to −57 mV and reduced R_{in} from 145 to 51 MΩ. The magnitude of the current shift is a simple consequence of Ohm's law ($\Delta i_{leak} = g_{leak} \times \Delta E_{leak}$ = 3 nS × {−50 mV} = −150 pA). The drop in R_{in} arises from the increased slope of the *I-V* relation at its new point of intersection with the zero current axis (Fig. 3*C*).

The general nonlinear dependence of V_{rest} on leak conductance and selectivity was mapped by systematically varying each parameter (Figs. 3*D* and 4). V_{rest}, defined as the point where I_{ionic} = 0, usually lies in the curved region of the steady-state *I-V* relation, at the balance point between voltage-insensitive inward leak current and voltage-sensitive outward M-current. The only exception occurs when E_{leak} is more negative than the activation range for g_M. When $E_{leak} \leq$ −80 mV, then $g_M \approx 0$ and V_{rest} converges at E_{leak}, regardless of g_{leak}'s magnitude (Fig. 3*D*). Otherwise, V_{rest} diverges as a nonlinear function of E_{leak} and g_{leak} (Fig. 3*D*). This raises a basic question. Given that leak current varies linearly with g_{leak} and E_{leak}, how can changing the leak parameters produce nonlinear shifts in V_{rest}? Because the model has only two conductances, the explanation must lie in the voltage dependence of g_M.

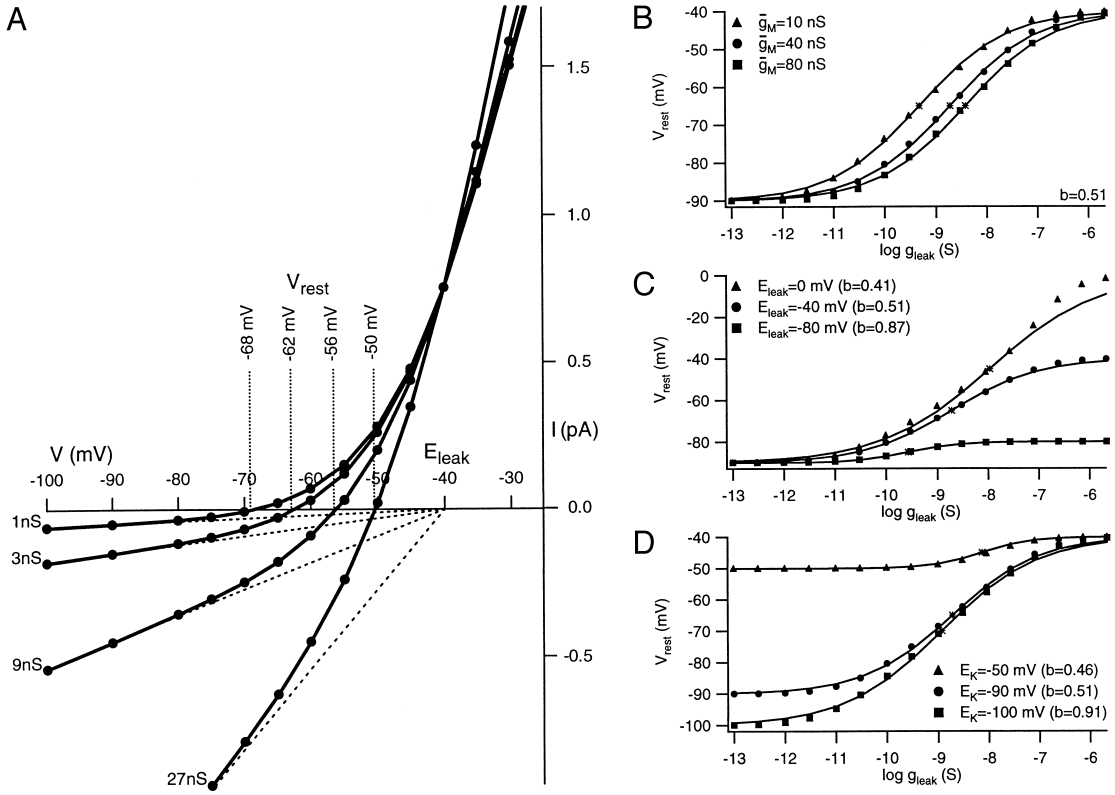

FIG. 4. Regulation of V_{rest} by g_{leak}. *A*: 3-fold increments in g_{leak} tend to linearize the steady-state *I-V* relation and cause it to rotate around E_{leak}. The geometric increase in g_{leak} depolarizes V_{rest} in constant 6-mV increments. Calculations based on the 2-conductance model ($\bar{g}_M$ = 40 nS, E_K = −90 mV, g_{leak} noted at the left of each relation). *B*: semi-logarithmic plot shows that changes in $\bar{g}_M$ produce parallel shifts in the sigmoidal relation between g_{leak} and V_{rest}. E_{leak} controls the right asymptote (*C*), and E_K controls the left asymptote (*D*). Lines in *B–D* drawn according to *Eq. 13*, with *b* as noted.

Activation of M-current introduces curvature into the steady-state *I-V* relation, and this curvature accounts for all nonlinearity in the control of V_{rest}. We have already shown how a selective change in E_{leak} produces a purely parallel shift of the *I-V* relation and alters its intersection with the zero-current axis (Fig. 3*C*). In this manner, the inherent curvature of the *I-V* relation dictates the nonlinearity between E_{leak} and V_{rest}. The effect of selectively changing g_{leak} is more complicated. Altering g_{leak} causes the slope of the leak current to rotate around E_{leak}, and the entire steady-state *I-V* relation changes shape as it rotates around E_{leak} (Fig. 4*A*). Increases in g_{leak} thus act to linearize the *I-V* relation.

Plotting V_{rest} as a logarithmic function of g_{leak} (Fig. 4*B*) revealed a sigmoidal relation with asymptotes at E_K and E_{leak}. Varying $\bar{g}_M$ (10, 40, and 80 nS) over its experimentally observed range (Adams et al. 1982; Jones 1989) produces a parallel shift in V_{rest} without altering its logarithmic dependence on g_{leak} in the experimentally relevant range. Figure 4*A* illustrates the point by showing that successive threefold increments in g_{leak} from 1 to 27 nS each depolarize V_{rest} by 6 mV. In other simulations, $\bar{g}_M$ was set to 40 nS, and we varied the equilibrium potential for each current. This demonstrated that E_{leak} controls the right asymptote of the sigmoidal relation (Fig. 4*C*) and that E_K controls the left asymptote (Fig. 4*D*). Although the two-conductance model becomes relatively simple in the steady-state, it does not have an easy analytic solution that can give the results obtained by numerical integration. We could, however, describe most of the numerical data by using a relatively simple empiric expression (*Eq. 13*). The midpoint along the *y*-axis was defined as V_{50}, the average of E_K and E_{leak} (*Eq. 14*). When $V_{rest} = V_{50}$ in the two-conductance model, it can be shown using *Eqs. 1* and *14* that $g_{leak} = g_M$. This conductance, defined as g_{L50}, can be calculated from *Eq. 15*, in which ω_{V50} (*Eq. 8*) is the steady-state activation of g_M at V_{50}. In *Eq. 13*, *b* is an arbitrary slope factor whose value was fit as a free parameter. The value of *b* changes with E_{leak} and E_K (Fig. 4, *C* and *D*)

$$V_{rest} = E_{leak} + \frac{(E_K - E_{leak})}{1 + \left(\frac{g_{leak}}{g_{L50}}\right)^b} \quad (13)$$

$$V_{50} = \frac{E_K + E_{leak}}{2} \quad (14)$$

$$g_{L50} = \omega_{V50}\bar{g}_M \quad (15)$$

By explaining the behavior of V_{rest}, the two-conductance model (Fig. 3*A*) can help in understanding the influence of electrode damage and muscarinic regulation of voltage-insensitive channels. Both mechanisms introduce additional leaks into the model (Fig. 1). Because the resting leak (g_{leak}), the damage leak (g_{elec}), and the muscarinic leak (g_{CNG}) are each passive by definition, they combine in a linear manner (*Eqs. 3* and *4*). One can therefore use the two-conductance model to predict the effects of recording damage and a muscarinic leak over a broad range of starting assumptions (Fig. 3*D*). In the

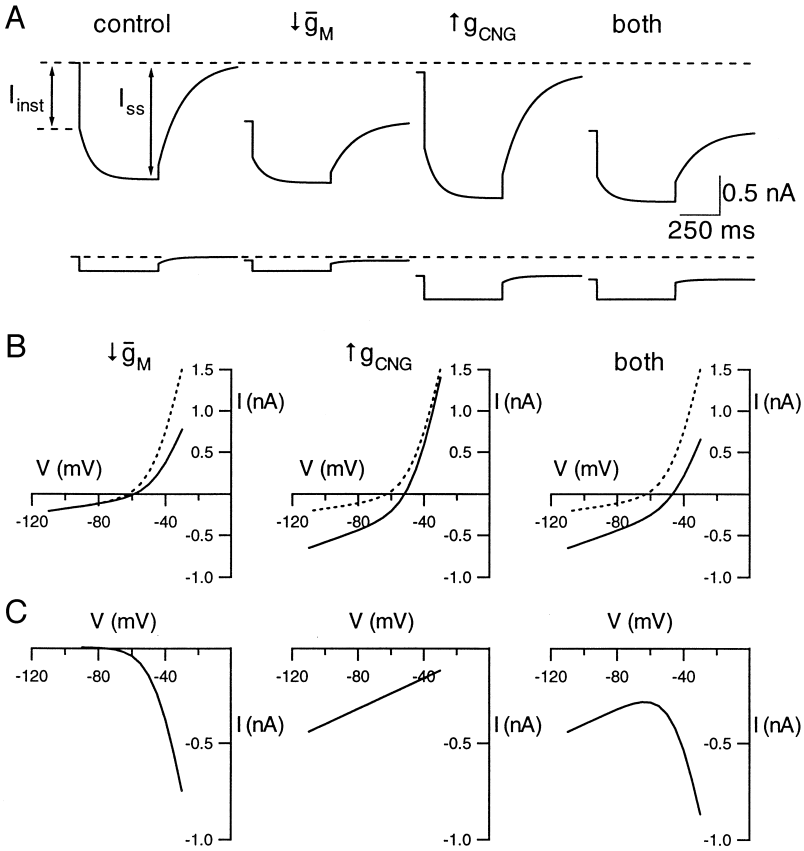

FIG. 5. Simulated muscarinic synaptic currents. *A*: voltage-clamp currents evoked by jumps from −30 to −60 mV (*top row*) and from −60 to −90 mV (*bottom row*) (control holding currents, – – –). Responses were calculated for a resting 2-conductance model (control; $\bar{g}_M$ = 40 nS, g_{leak} = 3 nS, E_{leak} = −40 mV) and after reducing $\bar{g}_M$ (50%), activating g_{CNG} (4 nS, E_{CNG} = 0 mV), and making both changes. *B*: steady-state *I-V* relations under control conditions (– – –) and for the 3 types of muscarinic excitation (—). *C*: synaptic current vs. voltage relations were obtained by subtracting muscarinic from control *I-V* relations. They reproduce experimental observations in 3 types of B neurons (compare with Fig. 1 in Tsuji and Kuba 1988).

following example and subsequent simulations, we used resting leak parameters (g_{leak} = 3 nS, E_{leak} = −40 mV) that lie at the boundary between patch and microelectrode data (Jones 1989; Tsuji and Kuba 1988). This sets V_{rest} = −62 mV (Fig. 3*D*, ○) and R_{in} = 85 M-Ω. Now we can consider an experiment in which g_{elec} = 2 nS and E_{elec} = 0 mV. Recording damage in this case would increase the $g_{leak-total}$ from 3 to 5 nS (*Eq. 3*) and shift $E_{leak-total}$ from −40 to −24 mV (*Eq. 4*). The consequence would be to depolarize V_{rest} by 7 mV and decrease R_{in} by 39 M-Ω. Identical changes would occur in a muscarinic response that activated 2 nS of nonselective cation conductance (i.e., g_{CNG}). The model shows how damage would mask one's ability to detect the muscarinic response in an experiment. The exponential relation between g_{leak} and V_{rest} reveals that increasing $g_{leak-total}$ from 5 to 7 nS will produce a smaller depolarization (3 mV) than the increase from 3 to 5 nS. With more recording damage (e.g., 10–20 nS) the muscarinic depolarization would become experimentally undetectable. Switching from current clamp to voltage clamp would not necessarily solve the problem. In the face of damage, the muscarinic current represents a lower fraction of the total leak, thereby lowering the signal-to-noise ratio. The important point is that very small increases in a muscarinic leak conductance can have potent effects, but only when they occur against the background of a low resting leak.

Form of pleiotropic muscarinic currents

Three forms of muscarinic excitation have been identified in frog B neurons and most clearly resolved in experiments by Tsuji and Kuba (1988). In one group of neurons, a dual-component muscarinic response is mediated by pleiotropic suppression of $\bar{g}_M$ (<50%) and activation of a cation conductance (<7 nS). In the other groups, only one component is found. It remains unclear whether this diversity reflects functional specialization in three types of B neurons or variations in recording damage. Before examining the consequences of pleiotropy, we needed to first reproduce the three forms of muscarinic currents (Fig. 5) in a model containing g_{leak}, g_M, and g_{CNG}.

Muscarinic depolarization of B neurons is slow, with an onset that takes seconds and a duration that can last minutes. For simplicity, we ignored the synaptic kinetics of slow muscarinic currents and simulated $\bar{g}_M$ and g_{CNG} at different constant levels. Figure 5 compares the membrane currents produced by 50% suppression of $\bar{g}_M$, by activation of 4 nS g_{CNG} (E_{CNG} = 0 mV), and by the combination of both. Figure 5*A* illustrates simulated clamp currents evoked by voltage jumps from −30 to −60 mV and from −60 to −90 mV. Responses in the more depolarized voltage range contain large M-currents, whereas those in the hyperpolarized range are dominated by leak current. Full steady-state *I-V* relations (Fig. 5*B*) were constructed by computing families of voltage jumps from a holding potential of −30 mV. Muscarinic synaptic currents were then obtained by subtracting the excited from control *I-V* relations (Fig. 5*C*) (for comparison with experimental data, see Fig. 1 in Tsuji and Kuba 1988).

Modulation of the nicotinic synapse and the emergence of synergy

Having captured the steady-state features of muscarinic pleiotropy, the model was expanded to include a fast nicotinic

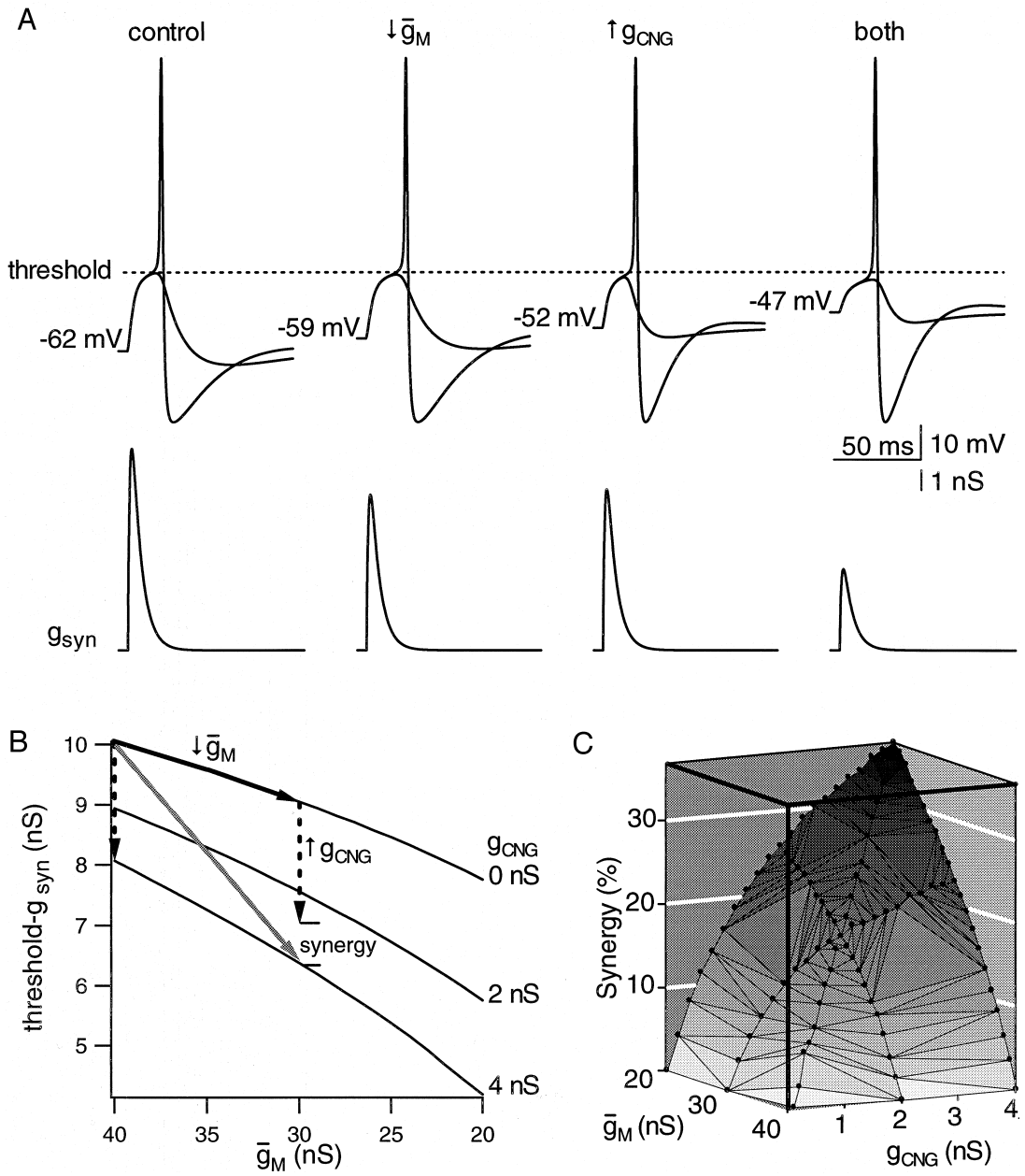

FIG. 6. Muscarinic potentiation of fast nicotinic transmission. Simulations computed with a 6-conductance model, which included nicotinic g_{syn} and an action potential (fast inactivating g_{Na}, delayed-rectifier g_K, threshold = −37 mV). *A*: g_{syn} was varied as a free parameter until the action-potential threshold was reached. This panel illustrates nicotinic EPSPs straddling threshold (*top traces*) and the associated threshold-g_{syn} (*bottom traces*) in the resting model (control; $\bar{g}_M$ = 40 nS, g_{leak} = 3 nS, E_{leak} = −40 mV) and during 3 types of muscarinic excitation. Suppressing $\bar{g}_M$ by 50% and increasing g_{CNG} by 4 nS produced similar reductions in threshold-g_{syn}. Combining both changes produced a 37% larger effect than the sum of the individual effects on threshold-g_{syn}. *B*: the nonlinear relation between threshold-g_{syn} and $\bar{g}_M$ at 3 levels of g_{CNG}. An example of vector addition illustrates synergy between the 2 muscarinic conductance changes. *C*: 3-dimensional plot of muscarinic synergy vs. $\bar{g}_M$ and g_{CNG}. Normalized synergy was calculated as the difference between threshold-g_{syn} for the combined conductance changes and that for the sum of individual effects, divided by the latter, and multiplied by 100.

EPSP with a realistic time course and an action potential with a realistic threshold (Figs. 1*B* and 2). The nicotinic synaptic conductance (g_{syn}) was then scaled until the resulting fast EPSP just barely crossed threshold and triggered an action potential. This was defined as the threshold synaptic conductance (Fig. 6*A*). Changes in threshold-g_{syn} were then measured to determine how different forms of muscarinic excitation altered the strength of nicotinic synapses. This revealed the potent excitatory effect of activating g_{CNG}. To cite a specific example in terms of the reduction in threshold-g_{syn}, a 4.65-nS increase in g_{CNG} was equivalent to suppressing $\bar{g}_M$ by 20 nS (Fig. 6*A*). More importantly, the combined effect of both conductance changes was greater than the sum of the individual effects. In other words, pleiotropic muscarinic excitation yields functional synergy when evaluated in terms of the consequences for fast synaptic transmission.

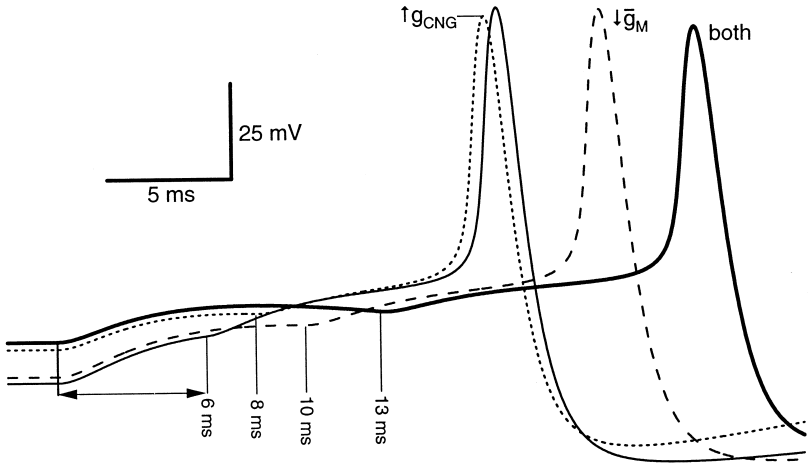

FIG. 7. Muscarinic enhancement of temporal summation between nicotinic EPSPs. Pairs of nicotinic EPSPs were computed using 55% threshold-g_{syn}. In the resting model ($\bar{g}_M$ = 40 nS, g_{leak} = 3 nS, E_{leak} = −40 mV), temporal summation triggered an action potential when the window of summation (t_{sum}) was ≤6 ms. Muscarinic stimulation lengthened the window of summation (4 nS g_{CNG}, t_{sum} ≤ 8 ms; 50% $\bar{g}_M$, t_{sum} ≤ 10 ms), and again, pleiotropy yielded synergy (t_{sum} ≤ 13 ms).

Is the synergy between suppression of g_M and activation of g_{CNG} a general property of metabotropic excitation? To answer this question we systematically varied g_{CNG} (0–4 nS) and $\bar{g}_M$ (100 to 50%) over their physiological ranges (Adams and Brown 1982; Kuba and Koketsu 1974; Tsuji and Kuba 1988). Figure 6*B* shows how threshold-g_{syn} decreased as $\bar{g}_M$ was suppressed at three different levels of g_{CNG}. When g_{CNG} was increased, so did the curvature of the relation. The simple graphic representation in Fig. 6*B* reveals that the combined effect of both conductance changes is always greater than the sum of the individual conductance changes, regardless of the initial and final conditions. When plotted in three dimensions (not shown), threshold-g_{syn} formed a smooth surface whose maximum (10.06 nS) was in the resting cell (0 nS g_{CNG}, 100% $\bar{g}_M$) and whose minimum (4.19 nS) was during full excitation (4 nS g_{CNG}, 50% $\bar{g}_M$). These data show the muscarinic decrease in threshold-g_{syn} and can effectively double the strength of nicotinic synapses. Using threshold-g_{syn} to calculate a synergy surface revealed a relation that resembled an upturned taco chip (Fig. 6*C*). The chip shows that maximal synergy (i.e., 37%) occurs when the muscarinic changes in both conductances are maximal.

The enhanced efficacy of the nicotinic synapse during muscarinic excitation was not simply a consequence of membrane depolarization. The decreases in threshold-g_{syn} produced by injecting current to mimic muscarinic depolarization were always smaller than those caused by $\bar{g}_M$ suppression and larger than those caused by activation of g_{CNG}. The effect has complex dynamics, but it can be explained qualitatively in terms of the steady-state *I-V* relation. In essence, all three types of depolarization produce different effects on R_{in}, which in turn influences the ability of a fast nicotinic current to drive the membrane potential to threshold. Depolarizing current injection produces a parallel shift in the *I-V* relation, like that produced by shifting E_{leak} (Fig. 3*C*). The consequence is a decrease in R_{in}, but not in the ultimate path to threshold. Equivalent depolarization can be produced by suppressing $\bar{g}_M$ (Fig. 5*B*), but in this case the overall slope conductance goes down. At the depolarized potential, R_{in} is less than it had been originally, but higher than in the cell depolarized by current injection. More importantly, reducing $\bar{g}_M$ increases membrane resistance along the entire voltage trajectory to threshold. The consequence is to enhance the efficacy or strength of fast synaptic currents. By contrast, increasing g_{CNG} produces a rotational effect, which increases the slope conductance at every point along the *I-V* relation (Fig. 4*A*) and thus makes the nicotinic current less effective than in the case of current injection. However, for small changes in the leak, the change in R_{in} is small, and the effect is not much different from that produced by current injection.

The synergy that emerges from muscarinic pleiotropy is a robust phenomenon that does not depend critically on the absolute magnitude of $\bar{g}_{Na}$ or $\bar{g}_K$. The balance between these conductances and the stimulus strength determines whether the model is inexcitable, fires once, fires repetitively and then accommodates, or fires repetitively without accommodation. Under our standard action potential parameters (Fig. 1*A*), the model was excitable and fired repetitively in response to strong muscarinic depolarization, but it always accommodated and became quiescent after a few action potentials. This reproduces the essential behavior of real B neurons. Over a range of conditions that give this pattern of excitability ($\bar{g}_{Na}$ = 600–4,200 nS and $\bar{g}_K$ = 1,500–3,500 nS), muscarinic pleiotropy always yielded synergy. One might imagine that muscarinic depolarization would increase inactivation of the delayed rectifier (*p*) or the sodium conductance (*h*) and thereby alter synergy. However, such effects turn out to be relatively minor. When *p* was removed from the model (Fig. 2, *C* and *E*), maximal synergy was 36%, a decrease of only 1%. The contribution of *h* was slightly larger and more complex. During the depolarization caused by maximal muscarinic excitation (e.g., Fig. 6), *h* decreased from 0.99 to 0.88. Simply eliminating *h* from the model made it unstable. Realistic excitability could be restored by decreasing $\bar{g}_{Na}$ or increasing $\bar{g}_K$. Raising $\bar{g}_K$ to 3,500 nS, while holding $\bar{g}_{Na}$ = 800 nS and keeping *h* and *p* intact, had little effect on the resting value of threshold-g_{syn}, which increased by <1%. Under these conditions maximal synergy was 33%, and when *h* was eliminated from the model, it increased to 39%. Taking the alternative tack of reducing $\bar{g}_{Na}$ while holding $\bar{g}_K$ constant confirmed that sodium channel inactivation has only a small influence on the magnitude of muscarinic synergy.

We next examined the consequences of regulating other leak conductances. In particular we evaluated the effects of increasing a chloride leak (g_{Cl}) and decreasing a potassium leak (g_{LK}). Both types of conductance changes have been observed during metabotropic stimulation of mammalian neurons (Bertrand and Galligan 1994; Cassell and McLachlan 1987; Caulfield 1993;

Marsh et al. 1995). Activating a 4-nS g_{Cl} (with $E_{Cl} = -40$ mV) decreased threshold-g_{syn} by 20.1% and yielded 37.6% synergy when combined with 50% suppression of $\bar{g}_M$. Removing 1 nS of g_{LK} from the standard resting leak (3 nS, $E_{leak} = -90$ mV) decreased threshold-g_{syn} by 12.2% and yielded 7.9% synergy when combined with 50% suppression of $\bar{g}_M$.

Muscarinic modulation of temporal interaction between nicotinic EPSPs

In addition to modulating the strength of nicotinic synapses, muscarinic excitation may influence the temporal summation of subthreshold nicotinic EPSPs. We examined this possibility by simulating the interaction between pairs of nicotinic EPSPs. For the simulation in Fig. 7, nicotinic g_{syn} was set to 55% threshold-g_{syn}. In the resting cell, the second nicotinic EPSP in a pair generated an action potential when the temporal window of summation (t_{sum}) was ≤6 ms. Combining 25% suppression of $\bar{g}_M$ (40 → 30 nS) with activation of 3 nS g_{CNG} more than doubled t_{sum} (≤13 ms). Selective changes in $\bar{g}_M$ or g_{CNG} each enhanced t_{sum} on their own, but once again the pleiotropic effect was greater than the sum of its parts (Fig. 7).

DISCUSSION

We have studied a minimal model of the frog B neuron after constraining it with experimental data. Only two conductances, g_{leak} and g_M, were needed to reproduce the resting behavior of the B neuron and explain its perturbation by recording damage and by pleiotropic muscarinic excitation. The central goal of the work was to determine how dual-component muscarinic excitation interacts with fast synaptic transmission to initiate postsynaptic firing. The results show that a small increase in cation conductance exerts potent excitatory effects, which can be obscured by modest recording damage. More importantly, muscarinic activation of the cation conductance combines synergistically with suppression of the M-conductance to strengthen nicotinic synapses and enhance temporal integration. The nonlinear effects unmasked by metabotropic regulation of leak currents are directly attributable to the voltage dependence of M-current. These results are discussed in terms of their implications for sympathetic function, their limitations, and their applicability to other cells and circuits. We begin by considering the rationale for taking a bottom-up approach.

Why study a minimal model?

Our model (Fig. 1*B*) is a cyber-knockout. We have deleted the Na^+ pump and seven conductances mediated by L-type Ca^{2+} channels, N-type Ca^{2+} channels, A-type K^+ channels, mini and maxi Ca^{2+}-activated K^+ channels, Q/H-type cation channels, and at least one type of voltage-dependent Na^+ channel. These mechanisms are all known to be present in frog B neurons, and indeed many were incorporated in an earlier computational model described by Yamada et al. (1989). The strophanthidin-sensitive pump current in B cells is 20 pA (Jones 1989). It hyperpolarizes V_{rest} in our model by 2 mV without producing significant consequences. The rationale for not including additional conductances was to keep the model simple and to avoid the unnecessary introduction of ad hoc assumptions. By doing so, it was possible to constrain all the parameters for resting and synaptic conductances with experimental data and to create an action potential that had realistic threshold behavior. Adding the other conductances would become important if one needed to consider repetitive firing. However, reproducing this behavior was not required to answer the first-order questions about muscarinic pleiotropy.

Two new principles emerged from the analysis. First, V_{rest} depends logarithmically on g_{leak} (Fig. 4). This helps to explain why estimates of V_{rest} in sympathetic neurons tend to be clustered in a fairly narrow range (i.e., −50 to −60 mV, Fig. 3*D*), irrespective of recording damage (Adams and Harper 1995; Karila and Horn 2000). Second, metabotropic changes in i_{leak} and i_M combine synergistically to modulate fast excitatory transmission (Figs. 6 and 7). The synergistic effects are not limited to cation leaks, but can also arise from an increased chloride leak or a decreased K^+ leak.

Can the model apply elsewhere?

We have hypothesized that the regulated leak conductance in frog B neurons is a cyclic GMP–gated cation channel (Fig. 1*A*). Adding a molecular dimension to the model was not essential from the computational point of view. Instead, it serves to create a fingerprint for identifying homologous mechanisms in other cells. In hippocampal CA1 pyramidal neurons, for example, m1 muscarinic receptors and metabotropic gluR5 glutamate receptors are coupled to the $G_{q/11}$ signaling pathway and may each regulate g_M and g_{CNG} (Conn and Pin 1997; Kingston et al. 1996; Marino et al. 1998). Do these conductances also interact synergistically in the hippocampus to strengthen fast glutamatergic transmission? Obviously one cannot say. Hippocampal neurons have a complex electrotonic structure, and their firing properties are more complicated than in our model. Nonetheless, it would be interesting to know whether the model contains a kernel that is preserved in other guises.

Implications for sympathetic circuit function

Although the pleiotropic nature of slow muscarinic and peptidergic EPSPs in sympathetic neurons has been appreciated for some time, the functional significance of these mechanisms for ganglionic integration remains largely unknown (Akasu et al. 1984; Jones 1985; Katayama and Nishi 1982; Kuba and Koketsu 1974; Kuffler and Sejnowski 1983; Tsuji and Kuba 1988). Ever since the discovery of M-current, most attention in the field has been focused on the ability of slow EPSPs to enhance repetitive firing by reducing accommodation. As it turns out, this effect depends on another conductance change that acts in concert with $\bar{g}_M$ suppression, and it is not limited to sympathetic neurons. Muscarinic agonists stimulate repetitive firing in sympathetic neurons and cortical pyramidal cells by inhibiting M-current and the afterhyperpolarization (AHP) current (Adams et al. 1986; Caulfield 1993; Cole and Nicoll 1983; Goh and Pennefather 1987; McCormick and Prince 1986; Nicoll et al. 1990). In frog B neurons, the action potential has a long hyperpolarizing afterpotential that is controlled by low-conductance Ca^{2+}-activated K^+ channels (g_{AHP}). The g_{AHP} does not contribute to V_{rest} or the slow EPSP, but it is inhibited by muscarinic agonists and luteinizing hormone releasing hormone (LHRH) (Adams et al. 1986). In what appears to be another case of synergy, the metabotropic

changes in i_M and i_{AHP} combine to regulate the accommodation of repetitive firing during sustained depolarization (Goh and Pennefather 1987).

The potent influence of muscarine and LHRH on accommodation led to an earlier proposal that slow synaptic regulation of repetitive firing molds ganglionic amplification of activity (Horn 1992). However, experiments to test this hypothesis in the secretomotor B system and the vasomotor C system have shown that synaptic regulation of repetitive firing is unlikely to occur under physiological conditions (Jobling and Horn 1996; Thorne and Horn 1997). This conclusion is buttressed by in vivo recordings, which show that frog B and C neurons fire in irregular patterns at low average frequencies (Ivanoff and Smith 1995).

Recently, a new theory of ganglionic integration has been developed from the analysis of subthreshold fast nicotinic EPSPs in frog B neurons and the irregular nature of preganglionic activity patterns in vivo (Karila and Horn 2000). Until these experiments, it had been widely believed that B neurons receive their nicotinic innervation through a single primary synapse. This created a paradox because primary synapses are very strong and generate fast EPSPs that inevitably drive B cells to fire action potentials. How then could muscarinic modulation influence nicotinic transmission? The recent experiments make clear that virtually all B neurons receive a small number of secondary nicotinic synapses that drive subthreshold fast synaptic activity (Karila and Horn 2000). Secondary fast EPSPs can reach threshold through temporal summation and interaction with slow EPSPs. However, it remains difficult to assess experimentally the strength of secondary synapses and to resolve how they are amplified by individual components of a slow EPSP. The conductance-based model enabled us to simulate these interactions in detail while setting aside the presynaptic facilitation and inhibition that further complicate experimental analysis (Karila and Horn 2000; Shen and Horn 1995, 1996). The model predicts that postsynaptic muscarinic excitation can more than double the strength of nicotinic synapses by reducing threshold-g_{syn} from 10.06 to 4.19 nS (Fig. 6*B*). This is encouraging because one would expect secondary nicotinic conductances to fall within this range based on the independent experimental analysis of synaptic currents and quantal content (Karila and Horn 2000; Shen and Horn 1995). More importantly, the present results suggest that realistic levels of muscarinic excitation are sufficient to boost subthreshold secondary nicotinic EPSPs above threshold (Fig. 6) and to enhance the temporal window for suprathreshold summation (t_{sum}; Fig. 7). In the context of a stochastic model of ganglionic integration (Karila and Horn 2000), these findings indicate that muscarinic excitation will enhance the activity-dependent synaptic amplification of preganglionic activity by sympathetic neurons. The synergy arising from muscarinic pleiotropy may function to make synaptic amplification more efficient.

We are especially grateful to B. Gutkin for helping initiate this work, and we thank G. B. Ermentrout, E. Frank, and E. Aizenman for reading the manuscript.

This work was supported by National Institute of Neurological Disorders and Stroke Grant NS-21065 and by Schrödinger Postdoctoral Fellowship J1519-BIO from the Austrian Science Fund to H. Schobesberger.

Address for reprint requests: J. P. Horn, Dept. of Neurobiology, University of Pittsburgh School of Medicine, E1440 Biomedical Science Tower, Pittsburgh, PA 15261.

Received 4 May 1999; accepted in final form 9 December 1999.

REFERENCES

ADAMS, D. J. AND HARPER, A. A. Electrophysiological properties of autonomic ganglion neurons. In: *Autonomic Ganglia*, edited by E. M. McLachlan. Reading, UK: Harwood Academic, 1995, p. 153–212.

ADAMS, P. R. AND BROWN, D. A. Synaptic inhibition of the M-current: slow excitatory post-synaptic potential mechanism in bullfrog sympathetic neurones. *J. Physiol. (Lond.)* 332: 263–272, 1982.

ADAMS, P. R., BROWN, D. A., AND CONSTANTI, A. M-currents and other potassium currents in bullfrog sympathetic neurons. *J. Physiol. (Lond.)* 330: 537–572, 1982.

ADAMS, P. R., JONES, S. W., PENNEFATHER, P., BROWN, D. A., KOCH, C., AND LANCASTER, B. Slow synaptic transmission in frog sympathetic ganglia. *J. Exp. Biol.* 124: 259–285, 1986.

AKASU, T., GALLAGHER, J. P., KOKETSU, K., AND SHINNICK-GALLAGHER, P. Slow excitatory post-synaptic currents in bull-frog sympathetic neurons. *J. Physiol. (Lond.)* 351: 583–593, 1984.

ARIANO, M. A., BRIGGS, C. A., AND MCAFEE, D. A. Cellular localization of cyclic nucleotide changes in rat superior cervical ganglion. *Cell. Mol. Neurobiol.* 2: 143–156, 1982.

BERTRAND, P. AND GALLIGAN, J. Contribution of chloride conductance increase to slow EPSC and tachykinin current in guinea-pig myenteric neurones. *J. Physiol. (Lond.)* 481: 47–60, 1994.

BLOCK, B. M. AND JONES, S. W. Ion permeation and block of M-type and delayed rectifier potassium channels. Whole-cell recordings from bullfrog sympathetic neurons. *J. Gen. Physiol.* 107: 473–488, 1996.

BRIGGS, C. A., WHITING, G. J., ARIANO, M. A., AND MCAFEE, D. A. Cyclic nucleotide metabolism in the sympathetic ganglion. *Cell. Mol. Neurobiol.* 2: 129–141, 1982.

BROWN, D. A., ABOGADIE, F. C., ALLEN, T. G., BUCKLEY, N. J., CAULFIELD, M. P., DELMAS, P., HALEY, J. E., LAMAS, J. A., AND SELYANKO, A. A. Muscarinic mechanisms in nerve cells. *Life Sci.* 60: 1137–1144, 1997.

BROWN, D. A. AND ADAMS, P. R. Muscarinic suppression of a novel voltage-sensitive K^+ current in a vertebrate neurone. *Nature* 283: 673–676, 1980.

CASSELL, J. F. AND MCLACHLAN, E. M. Muscarinic agonists block five different potassium conductances in guinea-pig sympathetic neurones. *Br. J. Pharmacol.* 91: 259–261, 1987.

CAULFIELD, M. P. Muscarinic receptors-characterization, coupling and function. *Pharmacol. Ther.* 58: 319–379, 1993.

COLE, A. E. AND NICOLL, R. A. Acetylcholine mediates a slow synaptic potential in hippocampal pyramidal cells. *Science* 221: 1299–1301, 1983.

COLE, A. E. AND NICOLL, R. A. Characterization of a slow cholinergic post-synaptic potential recorded in vitro from rat hippocampal pyramidal cells. *J. Physiol. (Lond.)* 352: 173–188, 1984.

CONN, P. J. AND PIN, J. P. Pharmacology and functions of metabotropic glutamate receptors. *Annu. Rev. Pharmacol. Toxicol.* 37: 205–237, 1997.

DESCARRIES, L., GISIGER, V., AND STERIADE, M. Diffuse transmission by acetylcholine in the CNS. *Prog. Neurobiol.* 53: 603–625, 1997.

DODD, J. AND HORN, J. P. A reclassification of B and C neurones in the ninth and tenth paravertebral sympathetic ganglia of the bullfrog. *J. Physiol. (Lond.)* 334: 255–269, 1983a.

DODD, J. AND HORN, J. P. Muscarinic inhibition of sympathetic C neurones in the bullfrog. *J. Physiol. (Lond.)* 334: 271–291, 1983b.

FRANKENHAEUSER, B. AND HUXLEY, A. F. The action potential in the myelinated nerve fibre of *Xenopus laevis* as computed on the basis of voltage clamp data. *J. Physiol. (Lond.)* 171: 302–315, 1964.

GOH, J. W. AND PENNEFATHER, P. S. Pharmacological and physiological properties of the after-hyperpolarization current of bullfrog ganglion neurones. *J. Physiol. (Lond.)* 394: 315–330, 1987.

HASHIGUCHI, T., USHIYAMA, N. S., KOBAYASHI, H., AND LIBET, B. Does cyclic GMP mediate the slow excitatory synaptic potential in sympathetic ganglia? *Nature* 271: 267–268, 1978.

HASSELMO, M. E. Neuromodulation and cortical function: modeling the physiological basis of behavior. *Behav. Brain Res.* 67: 1–27, 1995.

HORN, J. P. The integrative role of synaptic cotransmission in the bullfrog vasomotor C system: evidence for a synaptic gain hypothesis. *Can. J. Physiol. Pharmacol.* 70: S19–S26, 1992.

HORN, J. P. AND DODD, J. Monosynaptic muscarinic activation of K^+ conductance underlies the slow inhibitory postsynaptic potential in sympathetic ganglia. *Nature* 292: 625–627, 1981.

IVANOFF, A. Y. AND SMITH, P. A. In vivo activity of B- and C-neurones in the paravertebral sympathetic ganglia of the bullfrog. *J. Physiol. (Lond.)* 485: 797–815, 1995.

JOBLING, P. AND HORN, J. P. In vitro relation between preganglionic sympathetic stimulation and activity of cutaneous glands in the bullfrog. *J. Physiol. (Lond.)* 494: 287–296, 1996.

JONES, S. W. Muscarinic and peptidergic excitation of bull-frog sympathetic neurones. *J. Physiol. (Lond.)* 366: 63–87, 1985.

JONES, S. W. Sodium currents in dissociated bull-frog sympathetic neurones. *J. Physiol. (Lond.)* 389: 605–627, 1987.

JONES, S. W. On the resting potential of isolated frog sympathetic neurons. *Neuron* 3: 153–161, 1989.

KARILA, P. AND HORN, J. P. Secondary nicotinic synapses on sympathetic B neurons and their putative role in ganglionic amplification of activity. *J. Neurosci.* 20: 908–918, 2000.

KATAYAMA, Y. AND NISHI, S. Voltage-clamp analysis of peptidergic slow depolarizations in bullfrog sympathetic ganglion cells. *J. Physiol. (Lond.)* 333: 305–313, 1982.

KEBABIAN, J. W., BLOOD, F. E., STEINER, A. L., AND GREENGARD, P. Neurotransmitters increase cyclic nucleotides in postganglionic neurons: immunocytochemical demonstration. *Science* 190: 157–159, 1975a.

KEBABIAN, J. W., STEINER, A. L., AND GREENGARD, P. Muscarinic cholinergic regulation of cyclic guanosine 3,5-monophosphate in autonomic ganglia: possible role in synaptic transmission. *J. Pharmacol. Exp. Ther.* 193: 474–488, 1975b.

KINGSTON, P. A., ZUFALL, F., AND BARNSTABLE, C. J. Rat hippocampal neurons express genes for both rod retinal and olfactory cyclic nucleotide-gated channels: novel targets for cAMP/cGMP function. *Proc. Natl. Acad. Sci. USA* 93: 10440–10445, 1996.

KLEMIC, K. G., DURAND, D. M., AND JONES, S. W. Activation kinetics of the delayed rectifier potassium current of bullfrog sympathetic neurons. *J. Neurophysiol.* 79: 2345–2357, 1998.

KUBA, K. AND KOKETSU, K. Ionic mechanism of the slow excitatory postsynaptic potential in bullfrog sympathetic ganglion cells. *Brain Res.* 81: 338–342, 1974.

KUFFLER, S. W. AND SEJNOWSKI, T. J. Peptidergic and muscarinic excitation at amphibian sympathetic synapses. *J. Physiol. (Lond.)* 341: 257–278, 1983.

LAWRENCE, A. D. AND SAHAKIAN, B. J. The cognitive psychopharmacology of Alzheimer's disease: focus on cholinergic systems. *Neurochem. Res.* 23: 787–794, 1998.

LEVEY, A. I. Muscarinic acetylcholine receptor expression in memory circuits: implications for treatment of Alzheimer disease. *Proc. Natl. Acad. Sci. USA* 93: 13541–13546, 1996.

MADISON, D. V., LANCASTER, B., AND NICOLL, R. A. Voltage clamp analysis of cholinergic action in the hippocampus. *J. Neurosci.* 7: 733–741, 1987.

MARINO, M. J., ROUSE, S. T., LEVEY, A. I., POTTER, L. T., AND CONN, P. J. Activation of the genetically defined m1 muscarinic receptor potentiates *N*-methyl-D-aspartate (NMDA) receptor currents in hippocampal pyramidal cells. *Proc. Natl. Acad. Sci. USA* 95: 11465–11470, 1998.

MARRION, N. V. Calcineurin regulates M channel modal gating in sympathetic neurons. *Neuron* 16: 163–173, 1996.

MARRION, N. V. Control of M-current. *Annu. Rev. Physiol.* 59: 483–504, 1997.

MARSH, S. J., TROUSLARD, J., LEANEY, J. L., AND BROWN, D. A. Synergistic regulation of a neuronal chloride current by intracellular calcium and muscarinic receptor activation: a role for protein kinase C. *Neuron* 15: 729–737, 1995.

MATHES, C. AND THOMPSON, S. H. The nitric oxide/cGMP pathway couples muscarinic receptors to the activation of Ca^{2+} influx. *J. Neurosci.* 16: 1702–1709, 1996.

MCAFEE, D. A. AND GREENGARD, P. Adenosine 3′,5′-monophosphate: electrophysiological evidence for a role in synaptic transmission. *Science* 178: 310–312, 1972.

MCCORMICK, D. A. AND PRINCE, D. A. Mechanisms of action of acetylcholine in the guinea-pig cerebral cortex in vitro. *J. Physiol. (Lond.)* 375: 169–194, 1986.

NICOLL, R. A., MALENKA, R. C., AND KAUER, J. A. Functional comparison of neurotransmitter receptor subtypes in mammalian central nervous system. *Physiol. Rev.* 70: 513–565, 1990.

NISHI, S. AND KOKETSU, K. Early and late afterdischarges of amphibian sympathetic ganglion cells. *J. Neurophysiol.* 31: 109–121, 1968.

PERRY, E., WALKER, M., GRACE, J., AND PERRY, R. Acetylcholine in mind: a neurotransmitter correlate of consciousness? *Trends Neurosci.* 22: 273–280, 1999.

SELYANKO, A. A. AND BROWN, D. A. Intracellular calcium directly inhibits potassium M channels in excised membrane patches from rat sympathetic neurons. *Neuron* 16: 151–162, 1996.

SELYANKO, A. A., HADLEY, J. K., WOOD, I. C., ABOGADIE, F. C., DELMAS, P., BUCKLEY, N. J., LONDON, B., AND BROWN, D. A. Two types of K(+) channel subunit, erg1 and KCNQ2/3, contribute to the M-like current in a mammalian neuronal cell. *J. Neurosci.* 19: 7742–7756, 1999.

SHEN, W. X. AND HORN, J. P. A presynaptic mechanism accounts for the differential block of nicotinic synapses on sympathetic B and C neurons by D-tubocurarine. *J. Neurosci.* 15: 5025–5035, 1995.

SHEN, W. X. AND HORN, J. P. Presynaptic muscarinic inhibition in bullfrog sympathetic ganglia. *J. Physiol. (Lond.)* 491: 413–421, 1996.

SHENG, H., GAGNE, G. D., MATSUMOTO, T., MILLER, M. F., FORSTERMANN, U., AND MURAD, F. Nitric oxide synthase in bovine superior cervical ganglion. *J. Neurochem.* 61: 1120–1126, 1993.

THOMPSON, S. H. Cyclic GMP-gated channels in a sympathetic neuron cell line. *J. Gen. Physiol.* 110: 155–164, 1997.

THORNE, R. AND HORN, J. P. Role of ganglionic cotransmission in sympathetic control of the isolated bullfrog aorta. *J. Physiol. (Lond.)* 498: 201–214, 1997.

TOSAKA, T., CHICHIBU, S., AND LIBET, B. Intracellular analysis of slow inhibitory and excitatory postsynaptic potentials in sympathetic ganglia of the frog. *J. Neurophysiol.* 31: 396–409, 1968.

TRIVEDI, B. AND KRAMER, R. H. Real-time patch-cram detection of intracellular cGMP reveals long-term suppression of responses to NO and muscarinic agonists. *Neuron* 21: 895–906, 1998.

TSUJI, S. AND KUBA, K. Muscarinic regulation of two ionic currents in the bullfrog sympathetic neurone. *Pflügers Arch.* 411: 361–370, 1988.

WANG, H. S., PAN, Z., SHI, W., BROWN, B. S., WYMORE, R. S., COHEN, I. S., DIXON, J. E., AND MCKINNON, D. KCNQ2 and KCNQ3 potassium channel subunits: molecular correlates of the M-channel. *Science* 282: 1890–1893, 1998.

WEIGHT, F. F., PETZOLD, G., AND GREENGARD, P. Guanosine 3′,5′-monophosphate in sympathetic ganglia: increase associated with synaptic transmission. *Science* 186: 942–944, 1974.

WEIGHT, F. F., SMITH, P. A., AND SCHULMAN, J. A. Postsynaptic potential generation appears independent of synaptic elevation of cyclic nucleotides in sympathetic neurons. *Brain Res.* 158: 197–202, 1978.

WINKLER, J., THAL, L. J., GAGE, F. H., AND FISHER, L. J. Cholinergic strategies for Alzheimer's disease. *J. Mol. Med.* 76: 555–567, 1998.

YAMADA, W. M., KOCH, C., AND ADAMS, P. R. Multiple channels and calcium dynamics—modeling bullfrog sympathetic ganglion cells. In: *Methods in Neuronal Modeling: From Synapses to Networks*, edited by C. Koch and I. Segev. Cambridge, MA: MIT Press, 1989, p. 97–133.